Impact, Thermal, and Morphological Properties of Functionalized Rubber Toughened-Poly(ethylene terephthalate) Nanocomposites

S. R. Lim, W.S. Chow

School of Materials and Mineral Resources Engineering, Engineering Campus, Universiti Sains Malaysia, 14300 Nibong Tebal, Pulau Pinang, Malaysia

ABSTRACT: In this study, poly(ethylene terephthalate)/organo-montmorillonite (PET/OMMT) nanocomposites were melt-compounded using twin screw extruder followed by injection molding. Maleic anhydride grafted styrene-ethylene/butylene-styrene (SEBS-g-MAH) was used to improve the impact properties of the PET/OMMT nanocomposites. The notched and un-notched impact strength of PET/OMMT nanocomposites increased at about 2.5 times and 5.5 times by the addition of 5 wt % of SEBS-g-MAH. Atomic force microscopy (AFM) scans were taken from the polished surface of both PET/OMMT and SEBS-g-MAH toughened PET/OMMT nanocomposites. The addition of SEBS-g-MAH altered the phase structure and clay dispersion in PET matrix. It was found that some of the OMMT silicate layers were encapsulated by SEBS-g-MAH. Further, the addition of SEBS-g-MAH decreased the degree of crystallinity of the PET/OMMT nanocomposites. © 2011 Wiley Periodicals, Inc. J Appl Polym Sci 123: 3173–3181, 2012

Key words: polyesters; clay; nanocomposites; impact properties; atomic force microscopy

INTRODUCTION

The researches on the polymer/clay nanocomposites have attracted much academic and industrial attention. PET/clay nanocomposites often exhibit outstanding performances attributed to the high aspect ratio and exfoliation-ability of the clay layered silicates. The development of PET/clay hybrid has allowed the production of light weight nanocomposites with only a small amount of clay loading (<5 wt %). The typical enhanced properties include high thermal stability,[1–4] excellent mechanical properties,[5–9] improved flame retardancy,[10,11] and reduced gas permeability.[12–15]

From the literature, it was found that PET/clay nanocomposites could exhibit superior stiffness and modulus over neat PET. Nevertheless, the impact strength and ductility of PET generally reduced after adding clay.[16–20] It is known that the toughening of polymer/clay nanocomposites can be achieved by incorporating impact modifier and functionalized rubber. Numerous researches have been done on polymer/clay nanocomposites, e.g., polyamide (PA),[21–23] polypropylene (PP),[24] high density polyethylene (HDPE),[25] polycarbonate (PC),[26] PET,[27] and other polymer blends.[28,29]

PET and its composites are widely involved in various engineering applications where they are frequently deformed at high strain rates under impact loading during their service lives. Blending of PET with SEBS had been proven as one of the strategies for promoting enhanced toughness.[30] Further, the introduction of maleic anhydride functionalized SEBS was reported to act as emulsifier that improved adhesion between the phases and promoted better dispersion of the elastomer in the melt. This leads to the change in the fracture mechanism of PET from crazing to cavitation or shears yielding, and even reduces notch sensitivity effectively.[30–34]

In this work, PET nanocomposites filled with 3 wt % of OMMT were prepared by melt intercalation technique. PET/3 wt % clay nanocomposites demonstrating a balance of mechanical and thermal properties.[6,35,36] The aim of this article was to investigate the effects of SEBS-g-MAH concentration (5–20 wt %) on the impact and thermal properties of PET/OMMT nanocomposites. Atomic force microscopy (AFM) is a potential technique to study the

microstructure and nanostructure of polymer nano-composites.[37] This article also reports on the AFM study of the morphology, topography, and clay dispersion in PET nanocomposites.

EXPERIMENTAL

Materials

The PET (grade G084A) was purchased from MPI Polyester Industries, Malaysia. The OMMT (Nanomer 1.30TC) was supplied by Nanocor, USA. The OMMT consists of $\sim$ 70% montmorillonite (MMT) and 30% octadecylamine intercalant. The mean dry particle size of Nanomer 1.30TC is 16–22 µm. SEBS triblock copolymer grafted with 0.9 wt % of maleic anhydride was purchased from Shanghai Jianqiao Plastic, China. The ratio of styrene to ethylene/butylene in the triblock copolymer is 30 : 70. The glass transition temperature (T_g), melting temperature (T_m), and crystallization temperature (T_c) of the SEBS-g-MAH are 54.5, 104.6, and 81.9°C, respectively.

Preparation of PET/OMMT nanocomposites

Prior to extrusion process, the OMMT powder, PET pellets, and SEBS-g-MAH granules were dehumidified by using vacuum oven at 100°C for 8 h. PET nanocomposites filled with 3 wt % of OMMT were prepared by melt intercalation technique. SEBS-g-MAH was mixed together with PET/OMMT during the compounding by twin screw extruder (PSM 30, Sino-Alloy Machine, Taiwan). The SEBS-g-MAH content in the PET/OMMT nanocomposites varied from 0 to 20 wt %. The materials are labeled as PET/OMMT/5S, PET/OMMT/10S, PET/OMMT/15S, and PET/OMMT/20S where the numerals denote the SEBS-g-MAH loading in wt %. The extrusion temperatures ranged from 225 to 250°C. The screw speed was set at 90 rpm. After extrusion, the extrudates were cooled in a water bath and pelletized. Drying before molding was performed at 100°C in vacuum oven for 8 h. Injection molding was carried out in a laboratory scale injection molding machine (RR/TSMP, Ray-Ran Test Equipment, UK). The barrel temperature was 260°C and the mold temperature 75°C.

Characterization of PET/OMMT nanocomposites

X-ray diffraction analysis

The X-ray diffraction (XRD) analysis of OMMT, PET, and all the nanocomposite specimens was performed using X′Pert Pro XRD system (PANalytical, Netherlands) with Ni-filtered CuK$_\alpha$ radiation (0.154 nm wavelength). Scanning was performed at 25°C with diffraction angle (2θ) ranged from 2 to 10° with 0.050° Δ2θ-step. The interlayer spacing of the OMMT was derived from the peak position (d_{001}-reflection) in the XRD diffractograms according to the Bragg's equation ($\lambda = 2d \sin \theta$). All the nanocomposites specimens were cut from the injection-molded impact bar.

Notched and un-notched charpy impact test

Charpy impact tests of both notched and unnotched specimens were carried out using a pendulum-type testing machine (Type 5101, Zwick, Germany) in accordance to ASTM 6110-04. The dimensions of sample are 62.5 mm × 12.7 mm × 3 mm (length × width × thickness). A notch with 2 mm depth was made for notched specimen. Five specimens were tested for each composition. The testing was performed with pendulum of 7.5 J with a velocity of 3.84 m/s.

2.3.3 Thermal properties of PET/OMMT nanocomposites

The thermal properties of PET/OMMT nanocomposites were characterized using differential scanning calorimeter (DSC, model DSC-6, Perkin Elmer, USA). Approximately 10 mg of the PET sample was sealed in an aluminium pan. The sample was heated from 30 to 280°C, held at 280°C for 1 min, and cooled from 280 to 30°C. The degree of crystallization (χ_c) of the PET nanocomposites was calculated using eq. (1).

$$\chi_c(\%) = \frac{\Delta H_f}{\Delta H_f^o \times w_{PET}} \times 100\% \qquad (1)$$

For PET/OMMT nanocomposites without SEBS-g-MAH, the w_{PET} was calculated using eq. (2).

$$w_{PET} = 1 - w_{OMMT} \qquad (2)$$

For PET/OMMT nanocomposites toughened with SEBS-g-MAH, the w_{PET} was calculated using eq. (3).

$$w_{PET} = 1 - w_{OMMT} - w_{SEBS-g-MAH} \qquad (3)$$

where ΔH_f is the enthalpy of fusion of the sample, ΔH_f^o is the enthalpy of a hypothetical 100% crystalline PET (140 J/g),[8] while w_{OMMT} and $w_{SEBS-g-MAH}$ are the weight fraction of OMMT and SEBS-g-MAH, respectively.

Morphological properties of PET/OMMT nanocomposites

Field emission scanning electron microscopy. The morphology of impact fractured surfaces of selected PET/OMMT nanocomposites was inspected in a field emission scanning electron microscope (FESEM, Supra 35VP, Zeiss, Germany). The fracture surfaces
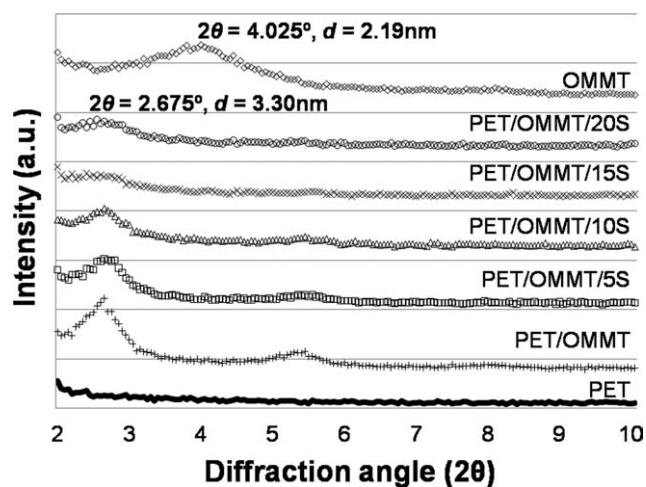
Figure 1 X-ray diffraction patterns of OMMT, PET, PET/OMMT, and PET/SEBS-g-MAH/OMMT nanocomposites.

were gold coated to avoid electrostatic charging during examination. The mean SEBS-g-MAH particle size was determined using ImageJ by taking the average out of 15 SEBS-g-MAH particles. Energy dispersive X-ray microanalysis (EDAX 32, Genesis) with accelerating voltage of 10 kV was used to analyze the occurrence of elements in the specimens that sputtered with gold.

Atomic Force Microscopy. Specimens were taken from the gauge section of injection molded specimen. The cross section surface, was first polished manually with silicon carbide paper up to 2000 Cw, and then mechanically polished using Al_2O_3 powder up to 0.05 μm (Imptech 10V Grinder-Polisher). Water was used as coolant throughout the polishing process. After rinsing with distilled water, the specimen was dried. The resulting surface was then scanned by atomic force microscope (AFM, SPA 400, SII Nano-Technology, Japan) equipped with SI-DF20 cantilever with aluminium back coating. The AFM was operated in dynamic force mode under an ambient atmosphere at room temperature. The scan range of the scanner used in this study was 20 μm × 20 μm ($x \times y$) and the height (z) is equal to or less than 1.5 μm.

RESULTS AND DISCUSSION

XRD analysis

Figure 1 shows the XRD diffratograms of OMMT and PET nanocomposites. It can be seen clearly that a diffraction peak was found at a 2θ of 4.025° (corresponding to the *d*-spacing of 2.19 nm) for the OMMT. As expected, the unfilled PET sample exhibited no visible diffraction peak in the range of 2θ = 2–10°. However the diffraction peaks of the PET nanocomposites shift toward a lower value of 2θ = 2.675°, which corresponding to the *d*-spacing of 3.30

nm. The observation of this peak indicates the presence of clay structure with expanded interlayer spacing. This is associated to the intercalation phenomenon. It is worth to emphasize that the diffraction peak becomes less intense with increasing SEBS-g-MAH loading. The substantial reduction in the intensities of the XRD peaks claims a better clay dispersion at higher SEBS-g-MAH loading.[6] This is owing to the MAH could act as an emulsifier to lower down the surface tension and thus more organic molecules were capable to penetrate into the galleries during melt compounding. This promotes an additional increase in the basal spacing of the silicate interlayer.

Impact properties of PET nanocomposites

Figure 2 shows the effects of SEBS-g-MAH content on the impact strength of PET/OMMT nanocomposites. It can be seen that the impact strength of PET reduced by the addition of OMMT. This indicates that the PET/OMMT nanocomposite possessed low impact strength due to the embrittlement effect of clay. It is recognized that the addition of high-stiffness silicate layers can reduce the toughness of nanocomposite attributed to the constraining effect[16,17] and lack of crack front deflection.[38] Interesting to note that, both notched and unnotched impact strength of PET/OMMT nanocomposites increased notably in the presence of SEBS-g-MAH. It can be seen that the PET/OMMT nanocomposites containing 5 wt % of SEBS-g-MAH exhibited the highest impact strength. In comparison to the PET/clay nanocomposite, the impact strength improved by 5.5 times for unnotched sample and about 2.5 times for sample in notched configuration with the
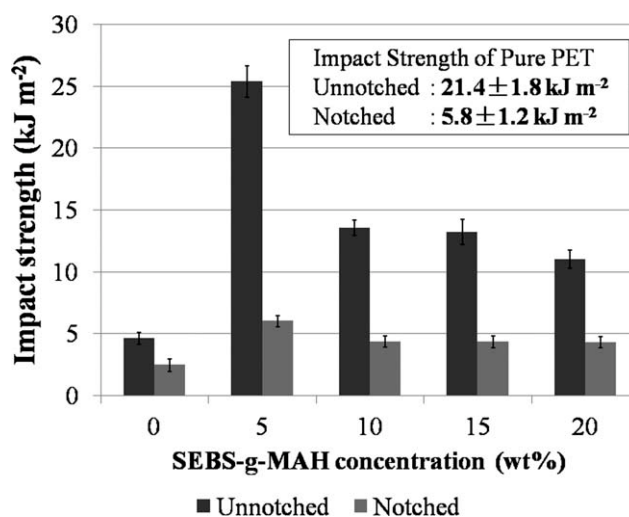
Figure 2 Notched and un-notched impact strength of PET/OMMT nanocomposites as a function of the SEBS-g-MAH content.
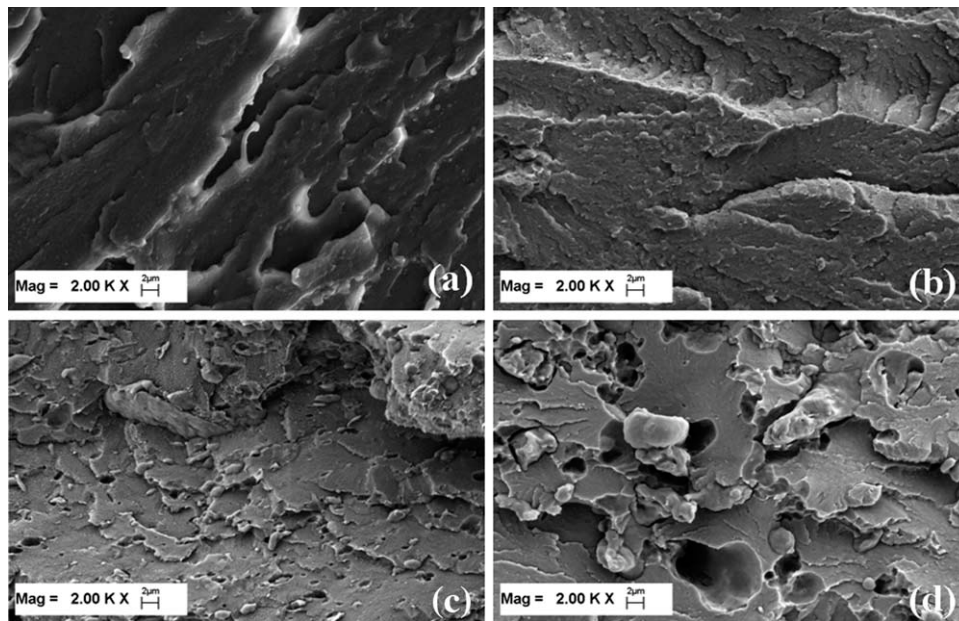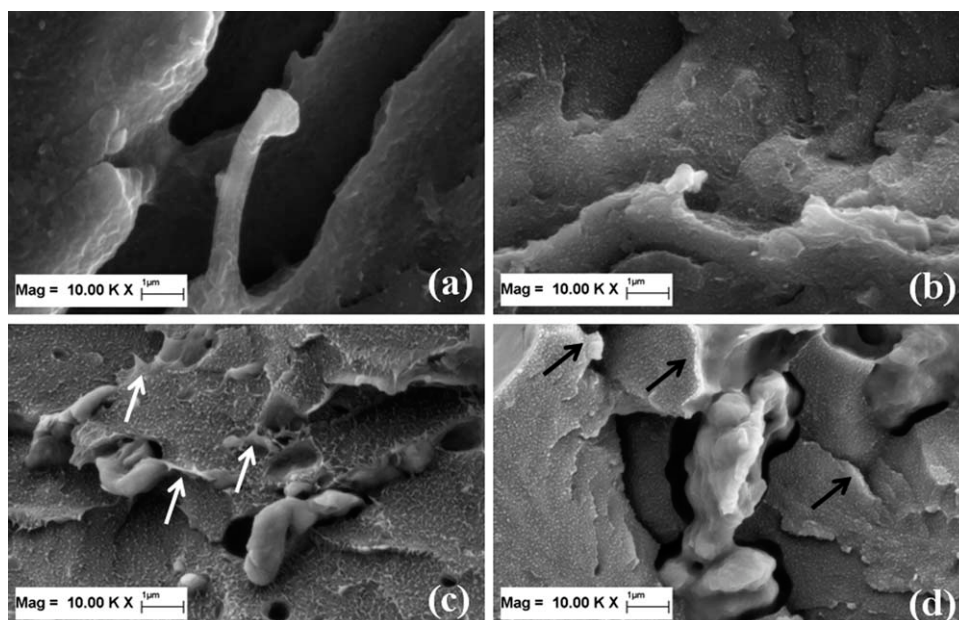
Figure 3 FESEM micrographs taken from the impact fractured surfaces of (a) unfilled PET, (b) PET/OMMT, (c) PET/OMMT/5S, and (d) PET/OMMT/20S nanocomposites at 2000× magnification.

inclusion of 5 wt % of SEBS-g-MAH. According to Alyamac and Yilmazer[27] the impact resistance of ethylene-methyl acrylate-glycidyl methacrylate impact modifier toughened PET/3% Cloisite 25A clay nanocomposites is 7.5 times higher than the PET/3% clay counterparts. As aforementioned, the presence of MAH acted as an emulsifier to decrease the interfacial tension. It has been well established that the reaction between the anhydride and the PET ester group or terminal -OH group resulted in

strong adhesion of PET and SEBS phases.[30,39] This allowed effective transfer of the applied load between SEBS particles and PET matrix and thus the resultant material was able to absorb more energy prior to fracture. Nonetheless, it should be noted that increasing of SEBS-g-MAH concentration (i.e., 10, 15, and 20 wt%) led to a gradual reduction in impact strength. This can be related to the excessive amount of SEBS-g-MAH. Hong et al.[40] reported that the reduction of toughness of PP/10wt% Cloisite

Figure 4 FESEM micrographs taken from the impact fractured surfaces of (a) unfilled PET, (b) PET/OMMT, (c) PET/OMMT/5S, and (d) PET/OMMT/20S nanocomposites at 10,000× magnification.

20A nanocomposites can be related to the high content of low molar mass MAH grafted PP compatibilizer. Refer to Figure 2, it can be seen that the extent of enhancement for notched samples was much lower than that for unnotched PET nanocomposites. It is known that the pre-existing notch would become stress concentration point and lower the energy absorption prior to fracture. In general, the presence of notch would change the nature of stress field from a biaxial stress to a critical triaxial stress ahead of the notch.[41] Tanrattanakul et al.[33] reported that under severe loading conditions with large triaxial component (e.g., notched impact test), larger number of cavitations were required to ensure a more efficient relief of the massive triaxiality stress. In other words, a much finer dispersion of SEBS particles and better interfacial adhesion between matrix and elastomers were a necessity to promote sufficient cavitation or a more extensive deformation in order to reduce the notch sensitivity of PET/OMMT system effectively.

Morphological properties of PET nanocomposites

SEM micrographs in Figure 3(a–d) show the FESEM micrographs taken from the impact fractured surface of PET, PET/OMMT, PET/OMMT/5S, and PET/OMMT/20S nanocomposites, respectively. It can be clearly seen that each of the specimen exhibited distinct fractographic features as well as fractured surface roughness. The fractured surface of pure PET demonstrated the stress whitening with some coarse fibrils whereas PET/OMMT sample failed in brittle mode with a little stress whitening band or crazing [Fig. 3(a,b)]. Comparatively, a more extensive deformation and rougher surface containing shear bands, micro-voids, and gaps that meandering through the matrix were observed on the fractured surface of the PET/OMMT constituted of SEBS-g-MAH [see Fig. 3(c,d)]. The microvoids and gaps were associated with the cavitation of SEBS particles or debonding of particle-matrix. According to Tjong,[42] cavitation of elastomer particles or debonding at the interface between particles and matrix was responsible for the impact strength improvement. The SEBS phase has comparatively lower modulus and hence it tends to void (e.g., cavitate or debond) upon application of stress. This is in consistent with the study of Loyens and Groeninckx[43] who investigated deformation behaviour of ethylene-co-propylene rubber (EPR) toughened PET. Void formation (cavitation/debonding) was observed when the released internally stored stress build-up (volumetric strain energy) is greater than the energy required for the creation and expansion of the surface area of the void.[43] The occurrence of void enabled the alteration of stress state of the surrounding matrix and allows an

overall deformation mechanism to take place. In particular, the cavities relieve the triaxial stress state in the region of the crack, thus creating a stress state beneficial for the initiation of multiple matrix shear yielding.[42,44] On account of the shear banded zones found on the fractured surface, it was attributed to the crack deflection and creation of additional surface area or new crack front at two different fracture planes. This would resulting in a higher impact resistant to the polymer composites owing to the fact that some amount of applied energy would certainly dissipated during the creation of the new fracture surface and new nonlinear crack front.[45]

On the other hand, Figure 3(c,d) as well as Figure 4(c,d) proved the PET/OMMT/5S sample displayed finer phase morphology as compared to the PET/OMMT/20S sample. By measurement, the mean size of SEBS-g-MAH dispersion phase in PET/OMMT/5S
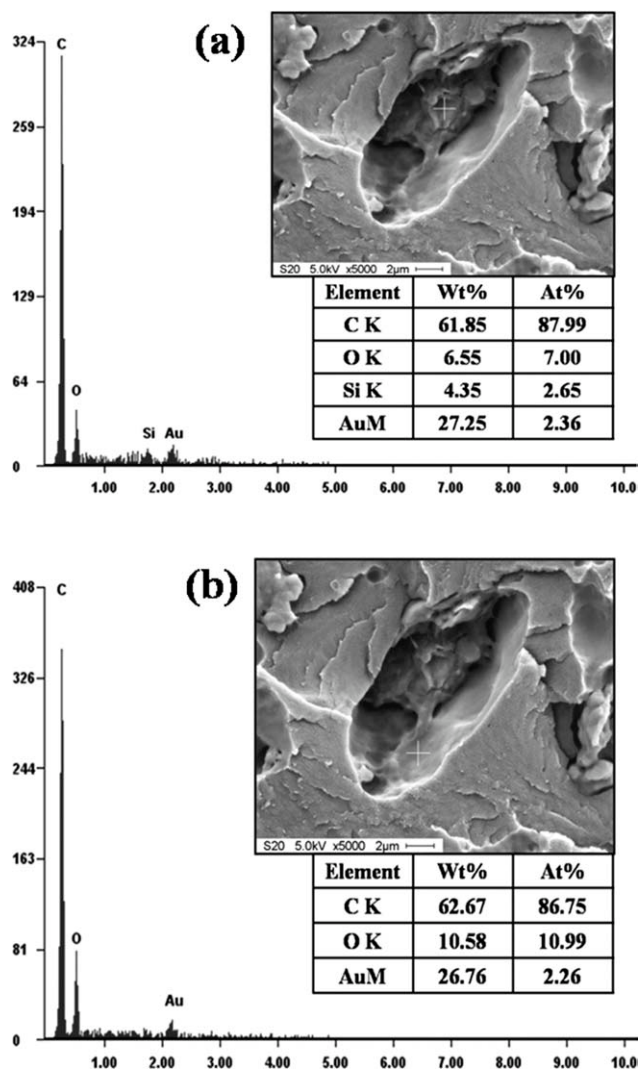
Figure 5 EDX taken from (a) the cavitated SEBS-g-MAH phase, and (b) the vicinity of SEBS-g-MAH phase on the fractured surface of PET/OMMT/5S nanocomposites.
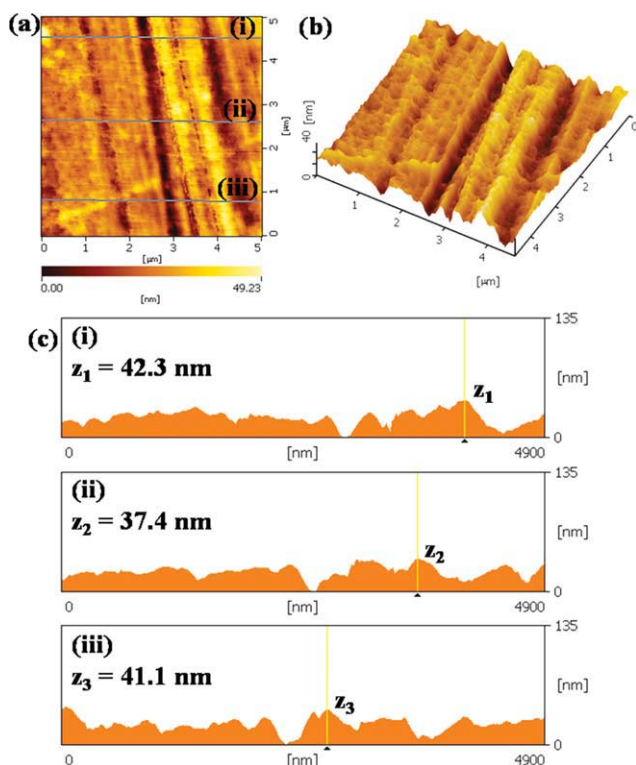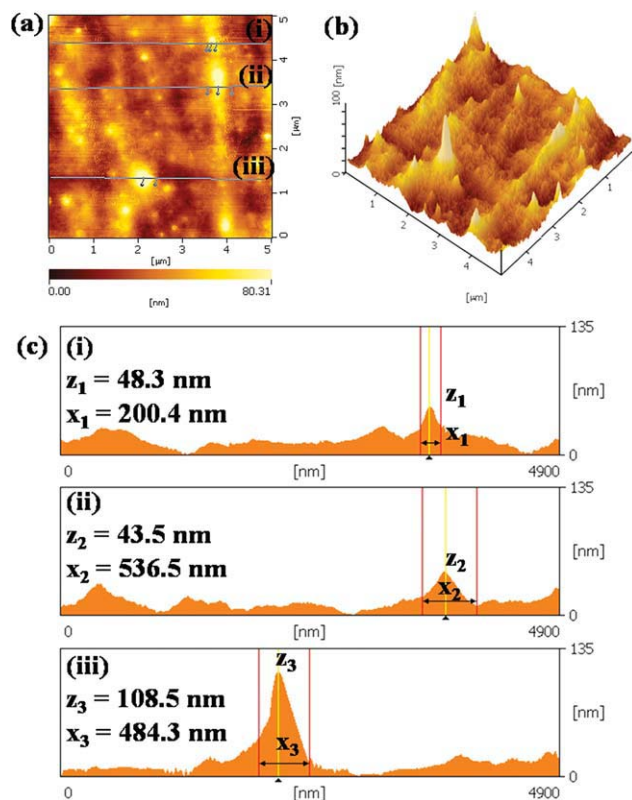
Figure 6 AFM images taken from the polished surface of unfilled PET nanocomposite. [Color figure can be viewed in the online issue, which is available at wileyonlinelibrary. com.]

is $\sim$ 0.9 μm whereas the one for PET/OMMT/20S is about 4.6 μm. This is in the expectation as the size of impact modifier could be bigger (i.e., occurrence of coalescence) with increasing SEBS-*g*-MAH content while the interparticle distance and surface area decreased accordingly. Recall that the PET/OMMT/ 5S exhibited the highest impact strength among all the PET/OMMT nanocomposites. The remarkable enhancement is believed to be associated with finer dispersion and larger surface area of SEBS, thereby improving its compatibility with PET.[32] In this case, greater portion of load exerted on the sample could be carried by the elastomeric particles, and thus increase the efficiency in toughening the resultant nanocomposites. The shear bands and a small number of tear morphology [as indicated by white arrow in Fig. 4(c)] were revealed on the fractured surface of PET/OMMT/5S nanocomposites. This can be correlated well with the significant improvement in impact strength. For PET/OMMT/20S specimen, its fractography illustrated in Figure 4(d) showed little shear banded zone with stress whitening [refer to black arrow in Fig. 4(d)] in the absence of tearing features. It is believed that the coarse and irregular shaped SEBS particles found on the fractured surface of PET/OMMT/20S specimen could act as defects. This explained the reduction in surface roughness and also impact resistant of the corresponding system.

Figure 5(a) shows the EDX taken from the cavitated SEBS-*g*-MAH rubber particle on the fracture surface of PET/OMMT/5S specimen. It is interesting to discover that Si element was found in the SEBS-*g*-MAH region. This result suggested that the clay materials were likely to disperse in SEBS-*g*-MAH, or possibly, the OMMT was encapsulated by the SEBS-*g*-MAH. This indicates the affinity and possible interfacial interaction between the OMMT and polar anhydride group of SEBS. However, in order to attain the maximum reinforcement effect, Yu et al.[46] reported that the preferable microstructure for toughness improvement is to have the maximum percentage of exfoliated organoclay in the continuous matrix rather than to have it in the dispersed functionalized rubber phase. Another EDX was taken at the vicinity near the SEBS-g-MAH, note that only carbon and oxygen elements were detected [c.f. Fig. 5(b)]. This can be ascribed to the PET matrix. From here, it is proposed that clay materials were more preferable to be situated in the SEBS particles instead of the PET matrix.

AFM studies

AFM has been recognized as one of the powerful tools for the analysis of surface morphologies as it

Figure 7 AFM images taken from the polished surface of PET/OMMT nanocomposite. [Color figure can be viewed in the online issue, which is available at wileyonlinelibrary. com.]
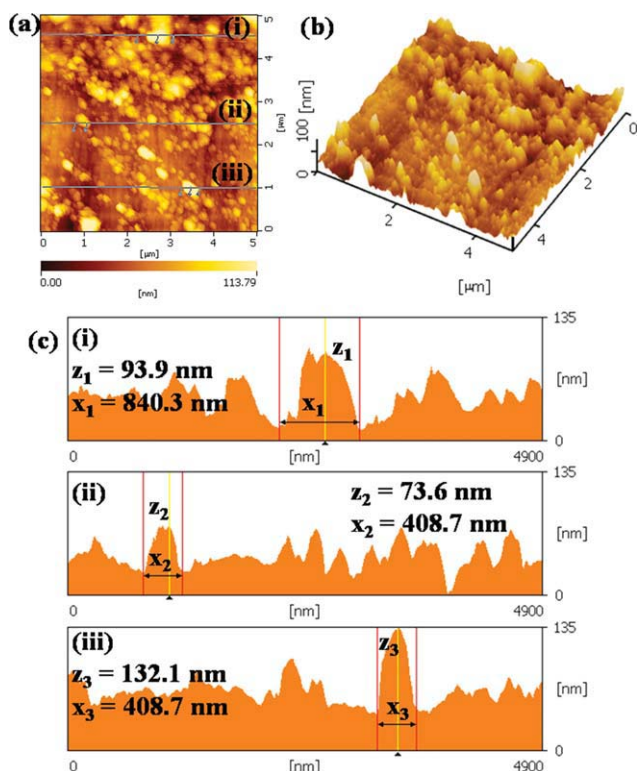
Figure 8 AFM images taken from the polished surface of PET/OMMT/5S nanocomposite. [Color figure can be viewed in the online issue, which is available at wileyonlinelibrary.com.]

creates three-dimensional images on the surface topography of samples and characterized surface roughness at an angstrom scale. Figures 6, 7, and 8 presented AFM images captured from the polished surface of unfilled PET, PET/OMMT, and PET/OMMT/5S nanocomposite respectively. Refer to Figure 6, it could be seen that the unfilled PET demonstrated a relatively flat surface topography in the absence of distinctive features as compared with Figures 7 and 8. For the PET/OMMT specimen, it is believed that the clay has higher ablation resistance than PET matrix, therefore the bright peaks in Figure 7(a,b) could be assigned as the protruded clay layers. From Figure 7(c), it can be seen that the height of the peaks are about 45–100 nm, this can be associated to the length of the silicate layer. Considering that the

aspect ratio (i.e., the length-to-thickness ratio) of the organoclay is about 200, it may suggest that the topography is due to the well-distributed embedment of the clay particles.[37] Further, the introduction of 5 parts of SEBS-g-MAH into PET/OMMT nanocomposites notably altered the blend morphology. In observing morphology in Figure 8(a,b), a number of broader bright domains (or humps) were discovered. The domain shapes could be seen clearer from the cross line profiles as depicted in Figure 8(c) whereby broader humps were found instead of the sharp tip observed for PET/OMMT nanocomposites [c.f. Fig. 7(c)]. At this point, the domains with 0.4–0.8 μm length were slightly smaller than certain SEBS-g-MAH particles inspected from SEM micrograph. This is because some of the elastomer particles were deformed upon failure and thus elongated features could be found from the SEM micrograph. The absence of darker colored gap surrounding the domains implicated an intimate adhesion between the phases. In line with both the SEM and EDX results, the humps in PET/OMMT/5S were presumably to be the SEBS-g-MAH embedded OMMT. A similar finding was documented by Chow and coworkers[37] who used AFM to examine the phase structure and clay dispersion in both the maleated PP compatibilized and uncompatibilized PA6/PP/organoclay nanocomposites. According to Chow and Neoh,[26] most of the clay silicate layers were distributed at the edge of SEBS-g-MAH particle in the PC/SEBS-g-MAH/clay nanocomposites. This result was originated from the interaction between the polar anhydride functional groups grafted to SEBS and hydroxyl groups of clay presence at the edge surface. Similar finding was reported by Calcagno et al.[47] that the clay was more capable to segregate in areas where the PET and PP-MAH were located. Herein, the strong tendency of organoclay to be situated in SEBS humps in present study could be attributed to the affinity of clays towards the polar anhydride functional groups grafted to SEBS.

Thermal properties of PET nanocomposites

The DSC thermal characteristics of the PET and its nanocomposites taken from the first and second

TABLE I
DSC Thermal Characteristics of PET, PET/OMMT, and PET/SEBS-g-MAH/OMMT Nanocomposites

Sample	First scanning						Second scanning					
	T_g (°C)	T_m (°C)	ΔH_f (J/g)	ΔH_c (J/g)	T_c (°C)	χ_c (%)	T_g (°C)	T_m (°C)	ΔH_f (J/g)	ΔH_c (J/g)	T_c (°C)	χ_c (%)
Pure PET	69.2	251.6	36.0	35.6	189.3	25.7	77.8	246.6	33.7	35.1	189.4	24.1
PET/OMMT	69.2	253.1	37.9	35.4	205.1	27.9	79.5	248.3	36.8	33.2	200.3	27.1
PET/OMMT/5S	66.1	250.7	33.3	33.0	205.7	24.5	68.6	249.7	28.6	32.8	204.8	21.0
PET/OMMT/10S	66.3	252.4	33.0	32.4	204.1	24.2	67.4	250.2	27.3	31.6	205.4	20.0
PET/OMMT/15S	65.3	251.8	32.2	30.1	206.3	23.6	65.6	250.0	26.7	29.8	206.6	19.6
PET/OMMT/20S	57.0	251.3	31.9	25.5	204.4	23.4	57.5	250.2	26.4	23.9	204.2	19.3

scanning were summarized in Table I. As can be seen, the T_g values of PET nanocomposite decreased by around 20°C with the addition of 20 wt % of SEBS-g-MAH. This is attributed to the plasticizing effect of the elastomeric phase.[48] In addition, the decrease of T_g could be attributed to an increase in the amorphous volume fraction due to the reactive compatibilization[44] as well as reduction in the number of nuclei.[49] Plus, an excessive contents of SEBS-g-MAH would induce coalescence and negatively affects the compatibility between matrix and dispersing component. Therefore, the drastic drop in T_g could be ascribed to free volume existing at the matrix-particle interface due to poor interfacial contact for PET/OMMT/20S nanocomposites. On the other side, there is no remarkable change in T_m of the PET by the incorporation of OMMT as well as SEBS-g-MAH. Similar result was also reported by Kusmono et al.[29] where the addition of both the organoclay and the SEBS-g-MAH had negligible effect on the melting behavior of the PA6/PP nanocomposites. Concerning the T_c value, the incorporation of OMMT shifted the crystallization temperature from around 189°C to a higher temperature of 205.1°C (during the first cooling). Besides, an increase in χ_c had been found for PET/OMMT nanocomposite as compared with pure PET. Both of these points recognized the presence of inorganic nanoparticles would act as crystallization nuclei to initiate the growth of spherulites and accelerate the crystallization of PET matrix.[50,51] From Table I, it also can be seen that the enthalpies of crystallization, ΔH_c, of the PET/SEBS-g-MAH/OMMT declined to much lower values compared with the PET/OMMT nanocomposites. The decline in ΔH_c caused by the addition of SEBS-g-MAH could be anticipated with the reduction of bulk PET fraction.[52] In addition to ΔH_c, the degree of crystallinity (χ_c) of PET/OMMT nanocomposites decreased considerably in the presence of SEBS-g-MAH. This is due in the fact that the presence of SEBS-g-MAH restricted the crystallization of PET. The encapsulation of OMMT by SEBS-g-MAH reduces the nucleating efficiency of OMMT in PET/OMMT nanocomposites crystallization process. According to Chow and Lok,[53] the crystallinity of PLA/OMMT was reduced with the addition of maleated ethylene-propylene rubber indicated the kinetic restriction on the crystallization process. Furthermore, it was believed that the presence of rubber particles would not allow the growth of well developed lamellar crystals but rather acted as physical hindrance towards crystal formation.[54]

CONCLUSIONS

Based on this work devoted to study the effects of SEBS-g-MAH on the properties of PET nanocomposites, the following conclusions can be drawn:

The impact strength of PET/OMMT nanocomposites increased significantly by the addition of SEBS-g-MAH. However, excessive loading of SEBS-g-MAH would induce coalescence and generate large domains of irregular shapes which acted as defects that limited the enhancement of impact strength. The AFM technique is able to detect and characterize the dispersion of the OMMT and SEBS-g-MAH embedded silicate layers. The encapsulation of OMMT by SEBS-g-MAH influenced the crystallization temperature and degree of crystallinity of the PET nanocomposites.

References

1. Lai, M. C.; Chang, K. C.; Huang, W. C.; Hsu, S. C.; Yeh, J. M. J Phys Chem Solids 2008, 69, 1371.
2. Lee, S. S.; Ma, Y. T.; Rhee, H. W.; Kim, J. Polymer 2005, 46, 2201.
3. Patro, T. U.; Khakhar, D. V.; Misra, A. J Appl Polym Sci 2009, 113, 1720.
4. Wu, T. B.; Ke, Y. C. Polym Degrad Stabil 2006, 91, 2205.
5. Bizarria, M. T. M.; Giraldi, A. L. F. D. M.; De Carvalho, C. M.; Velasco, J. I.; D'Ávila, M. A.; Mei, L. H. I. J Appl Polym Sci 2007, 104, 1839.
6. Chang, J. H.; Kim, S. J.; Joo, Y. L.; Im, S. Polymer 2004, 45, 919.
7. Gurmendi, U.; Eguiazabal, J. I.; Nazabal, J. Macromol Mater Eng 2007, 292, 169.
8. Litchfield, D. W.; Baird, D. G. Polymer 2008, 49, 5027.
9. Sanchez-Solis, A.; Romero-Ibarra, I.; Estrada, M. R.; Calderas, F.; Manero, O. Polym Eng Sci 2004, 44, 1094.
10. Gianelli, W., Camino, G., Tabuani, D., Bortolon, V., Savadori, T.; Monticelli, O. Fire Mater 2006, 30, 333.
11. Morgan, A.B.; Harris, R. H., Jr.; Kashiwagi, T.; Chyall, L. J.; Gilman, J. W. Fire Mater 2002, 26, 247.
12. Choi, W. J.; Kim, H. J.; Yoon, K. H.; Kwon, O. H.; Hwang, C. I. J Appl Polym Sci 2006, 100, 4875.
13. Ke, Y.; Long, C.; Qi, Z. J Appl Polym Sci 1999, 71, 1139.
14. Zeng, K.; Bai, Y. P. Mater Lett 2005, 59, 3348.
15. Kim, S. H.; Kim, S. C. J Appl Polym Sci 2007, 103, 1262.
16. Frounchi, M.; Dourbash, A. Macromol Mater Eng 2009, 294, 68.
17. De Giraldi, A. L. F. M.; Bizarria, M. T. M.; Silva, A. A.; Velasco, J. I.; D'Ávila, M. A.; Mei, L. H. I. J Appl Polym Sci 2008, 108, 2252.
18. Chow, W. S.; Mohd Ishak, Z. A.; Karger-Kocsis, J.; Apostolov, A. A.; Ishiaku, U. S. Polymer 2003, 44, 7427.
19. Ha, S. R.; Rhee, K. Y.; Kim, H. C.; Kim, J. T. Colloids Surf A: Physicochem Eng Asp 2008, 313–314, 112.
20. Ngo, T.-D.; Ton-That, M.-T.; Hoa, S. V.; Cole, K. C. J Appl Polym Sci 2008, 107, 1154.
21. Akkapeddi, M. K. Polym Compos 2000, 21, 576.
22. Tjong, S. C.; Bao, S. P. J Polym Sci, Part B Polym Phys 2005, 43, 585.
23. Dasari, A.; Yu, Z.-Z.; Mai, Y.-W. Polymer 2005, 46, 5986.
24. Tjong, S. C.; Bao, S. P.; Liang, G. D. J Polym Sci, Part B: Polym Phys 2005, 43, 3112.
25. Tjong, S. C.; Bao, S. P. Compos Sci Technol 2007, 67, 314.
26. Chow, W. S.; Neoh, S. S. Polym-Plast Technol Eng 2010, 49, 62.
27. Alyamac, E.; Yilmazer, U. Polym Compos 2007, 28, 251.
28. Chow, W. S.; Bakar, A. A.; Mohd Ishak, Z. A.; Karger-Kocsis, J.; Ishiaku, U. S. Eur Polym J 2005, 41, 687.
29. Kusmono; Mohd Ishak, Z. A.; Chow, W. S.; Takeichi, T.; Rochmadi. Eur Polym J 2008, 44, 1023.

30. Tanrattabakul, V.; Hiltner, A.; Baer, E. Polymer 1997, 38, 2191.
31. Pawlak, A.; Perkins, W. G.; Massey, F. L.; Hiltner, A.; Baer, E. J Appl Polym Sci 1999, 73, 203.
32. Yu, Z.-Z.; Yang, M.-S.; Dai, S.-C.; Mai, Y.-W. J Appl Polym Sci 2004, 93, 1462.
33. Tanrattabakul, V.; Hiltner, A.; Baer, E. Polymer 1997, 38, 4117.
34. Tanrattabakul, V.; Perkins, W. G.; Massey, F. L.; Moet, A.; Hiltner, A.; Baer, E. J Mater Sci 1997, 32, 4749.
35. Hemzehlou, S.; Katbab, A. A. J Appl Polym Sci 2007, 106, 1375.
36. Ke, Y. C.; Yang, Z. B.; Zhu, C. F. J Appl Polym Sci 2002, 85, 2677.
37. Chow, W. S.; Mohd Ishak, Z. A.; Karger-Kocsis, J. J Polym Sci, Part B: Polym Phys 2005, 43, 1198.
38. Kusmono; Mohd Ishak, Z. A.; Chow, W. S.; Takeichi, T.; Rochmadi. Express Polym Lett 2008, 2, 655.
39. Chiu, H. T.; Hsiao, Y. K. J Polym Res 2006, 13, 153.
40. Hong, C. H.; Lee, Y. B.; Bae, J. W.; Jho, J. Y.; Nam, B. U.; Hwang, T. W. J Appl Polym Sci 2005, 98, 427.
41. Ogazi-Onyemaechi, B. C.; Leong, Y. W.; Hamada, H. J Appl Polym Sci 2010, 116, 132.
42. Tjong, S. C. Mater Sci Eng R 2006, 53, 73.
43. Loyens, W.; Groeninckx, G. Polymer 2003, 44, 4929.
44. Loyens, W.; Groeninckx, G. Polymer 2002, 43, 5679.
45. Zerda, A. S.; Lesser, A. J. J Polym Sci, Part B: Polym Phys 2001, 39, 1137.
46. Yu, Z. Z.; Hu, G. H.; Varlet, J.; Dasari, A.; Mai, Y. W. J Polym Sci, Part B: Polym Phys 2005, 43, 1100.
47. Calcagno, C. I. W.; Mariani, C. M.; Teixeira, S. R.; Mauler, R. S. Compos Sci Technol 2008, 68, 2193.
48. Biju, P. K.; Radhakrishnan Nair, M. N.; Thomas, G. V.; Gopinathan Nair, M. R. Mater Sci-Poland 2007, 25, 919.
49. Suh, D.; Lim, Y.; Park, O. Polymer 2000, 41, 8557.
50. Hao, J. Y.; Lu, X. H.; Liu, S. L.; Lau, S. K.; Chua, Y. C. J Appl Polym Sci 2006, 101, 1057.
51. Ou, C. F.; Ho, M. T.; Lin, J. R. J Polym Res 2003, 10, 127.
52. Pang, Y. X.; Jia, D. M.; Hu, H. J.; Hourston, D. J.; Song, M. Polymer 2000, 41, 357.
53. Chow, W. S.; Lok, S. K. J Therm Anal Calorim 2009, 95, 627.
54. George, S.; Varughese, K. T.; Thomas, S. Polymer 2000, 41, 5485.